A Current Ratio Model for Defect Diagnosis using Quiescent Signal Analysis

Chintan Patel, Ernesto Staroswiecki, Dhurva Acharyya, Smita Pawar, and Jim Plusquellic

Department of CSEE, University of Maryland, Baltimore County

Abstract

I_{DDQ} test has been used extensively both as defect reliability screen and as a defect diagnostic technique. However, the increase in subthreshold leakage currents in deep sub-micron technologies has reduced the effectiveness of I_{DDQ} in these applications. Quiescent Signal Analysis (QSA) is a novel diagnostic technique that uses I_{DDQ} measurements made at multiple supply pads on the Chip-Under-Test as a means of locating shorting defects in the layout. The use of multiple supply pads reduces the adverse effects of leakage current by scaling the total leakage current over multiple simultaneous measurements. In previous work, a resistance model for QSA was developed and demonstrated on a small circuit. In this paper, the weaknesses of the original QSA model are identified, in the context of a production power grid (PPG) and probe card model, and a new model is described. The new QSA algorithm predicts the position of the defect in the layout through the analysis of hyperbolic current ratio contours. SPICE simulation experiments are used to demonstrate the improved prediction accuracy of the new model on a portion of the PPG.

1.0 Introduction

I_{DDQ} has been a main-stream supplemental testing method for defect detection for more than a decade with many companies. With the advent of deep submicron technologies, the use of single-threshold I_{DDQ} technique results in unacceptable yield loss. Setting an absolute pass/fail threshold for I_{DDQ} testing has become increasingly difficult due to the increasing subthreshold leakage currents [1]. Current signatures [2], delta-I_{DDQ} [3] and ratio-I_{DDQ} [4] have been proposed as a means for calibrating for these high subthreshold leakages. These techniques rely on a self-relative or differential analysis, in which the average I_{DDQ} of each device is factored into the pass/fail threshold. However, these proposed forms of calibration are expected to become increasingly less effective over successive technology generations.

An alternative calibration strategy that may have better scaling properties is to distribute the total leakage current across a set of measurements. This is accomplished by introducing probing hardware that allows access to the individual supply port I_{DDQ} values. The method proposed in this work, called Quiescent Signal Analysis (QSA), is designed to exploit this type of leakage calibration for defect detection and as a means of providing information about the defect's location in the layout [5][6].

A resistance-based model for QSA was developed in previous works and simulation experiments were used to demonstrate the diagnostic capabilities of the QSA method on a small circuit [5][6]. In this paper, several weaknesses of the resistance-based model are uncovered from simulations of a production power grid (PPG). A current-ratio-based model is proposed and demonstrated to improve on defect localization accuracy of the original method. The new method requires the insertion of a Calibration transistor under each of the supply pads in the design that permits the shorting of the power and ground supply rails at points close to the substrate. The state of the Calibration transistors are controlled by scan chain flip-flops. The I_{DDQ}s obtained when the Calibration transistor is turned on are used to calibrate the I_{DDQ}s measured under a failing I_{DDQ} pattern. The calibration technique is shown to address several weaknesses of the previous model involving non-zero probe card resistance and irregular supply grid topologies. Current ratios, as opposed to absolute currents, are proposed as a means of dealing with variation in the value of defect currents. Simulation experiments demonstrate that the maximum prediction error is 574 units in a 5,000 by 5,000 unit area.

The paper is organized as follows. Section 2.0 describes related work. Section 3.0 gives a brief description of the original resistance-based QSA technique, identifies its weaknesses and describes a new model. Section 4.0 presents the details of the current-ratio-based QSA method. Section 5.0 gives experimental results. Section 6.0 gives our conclusions and areas of future research.

2.0 Background

Several diagnostic methods have been proposed based on I_{DDQ} measurements. In general, these methods produce a list of candidate faults from a set of observed test failures using a fault dictionary. The likelihood of each candidate fault can be determined by several statistical algorithms. For example, signature analysis uses the Dempster-Shafer theory, which is based on Bayesian statistics of subjective probability [7]. Delta-I_{DDQ} makes use of the concepts of differential current probabilistic signatures and maximum likelihood estimation [8]. Although these methods are

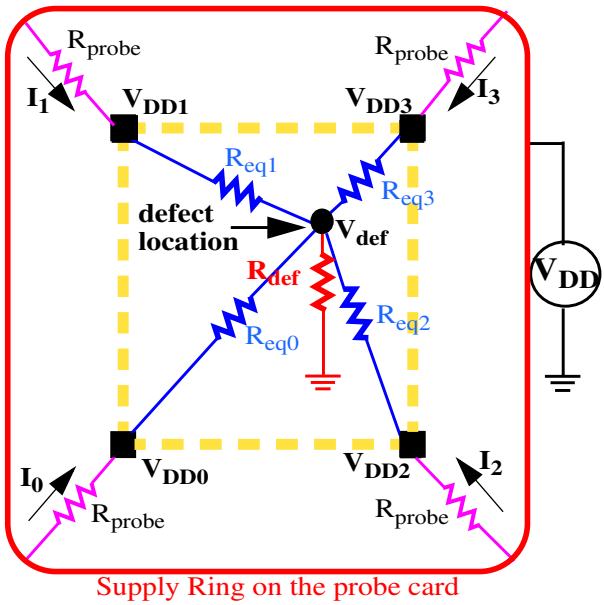

Figure 1. Equivalent resistance network with defect inside the circuit.

designed to improve the selection of fault candidates, in many cases, they are unable to generate a single candidate. Other difficulties of these methods include the effort involved in building the fault dictionary and the time required to generate the fault candidates from the large fault dictionary using tester data.

The QSA procedure can help in the selection of the most likely candidate from the candidate list produced by these algorithms. The physical layout information generated by our method can be used with information that maps the logical faults in the candidate lists to positions in the layout. In addition, it may be possible to use the (x,y) location information provided by QSA as a means of reducing the search space for likely candidates in the original fault dictionary procedure. This can reduce the processing time and space requirements significantly.

3.0 QSA Models

QSA analyzes a set of I_{DDQ} measurements, each obtained from individual supply pads from the Chip-Under-Test (CUT), to predict the location of a shorting defect. The resistive element of the power grid causes the current drawn by the defect to be non-uniformly distributed to each of the supply pads. In particular, the defect draws the largest fraction of its current from supply pads topologically "nearby". The same is true of the leakage currents. However, only the leakage currents in the vicinity of the defect contribute to the measured current in these pads. The smaller background leakage component improves the accuracy of the defect current measurement. As described in previous works, QSA also proposes the use of regression analysis as a means of eliminating the remaining leakage component from the measured values [5][6].

3.1 The Resistance-based QSA Model

The fraction of the defect current provided by each of the pads in the region of the defect is proportional to the equivalent resistance between the defect site and each of the pads. The differences in these values can be used to localize the defect using a method based on triangulation. Consider the resistance model of a simple power supply grid as shown in Figure 1. Here, R_{eq0} through R_{eq3} represent the equivalent resistances between each of the supply pads and the defect site shown in the center of the figure. The following set of equations describe the relationship between the power supply branch currents, I_0 through I_3 and V_{def}, the voltage at the defect site.

$$I_i \times (R_{eqi} + R_p) = V_{DD} - V_{def} \quad \text{for i} = 0,1,2,3$$

Eq. 1. System of equations for R_{eqi}.

In Eq. 1, I_i and R_p (the probe card's resistance) can be measured, whereas R_{eqi} and V_{def} are unknowns. Therefore, without additional information, it is not possible to solve these equations since there are 4 equations and 5 unknowns. However, for purpose of diagnosis, only the relationships between the R_{eqi} are needed. Relative equivalent resistances, R_{eqi}, can be computed with respect to a reference equivalent resistance, R_{eqj}, as given by Eq. 2.

$$I_i \times (R_{eqi} + R_p) = I_j \times (R_{eqj} + R_p)$$

solving for R_{eqi} in terms of R_{eqj} gives

$$R_{eqi} = \frac{I_j}{I_i} \times R_{eqj} + \left(\frac{I_j}{I_i} - 1\right) \times R_p \quad \text{with} \quad i \neq j$$

Eq. 2. Relative equivalent resistances.

Under either of the two conditions that R_p is small (with respect to R_{eqi}) or the value of R_{eqj} is 1, it is possible to obtain an accurate prediction of the defect's location by solving the circle expressions given in Eq. 3 for a common point of intersection given by x and y. The parameters h_i

$$k \times R_{eqj}(=1) = \sqrt{(x - h_j)^2 + (y - k_j)^2}$$

$$k \times R_{eqi_1} = \sqrt{\left(x - h_{i_1}\right)^2 + \left(y - k_{i_1}\right)^2}$$

$$k \times R_{eqi_2} = \sqrt{\left(x - h_{i_2}\right)^2 + \left(y - k_{i_2}\right)^2}$$

Eq. 3. Circle equations for triangulation.

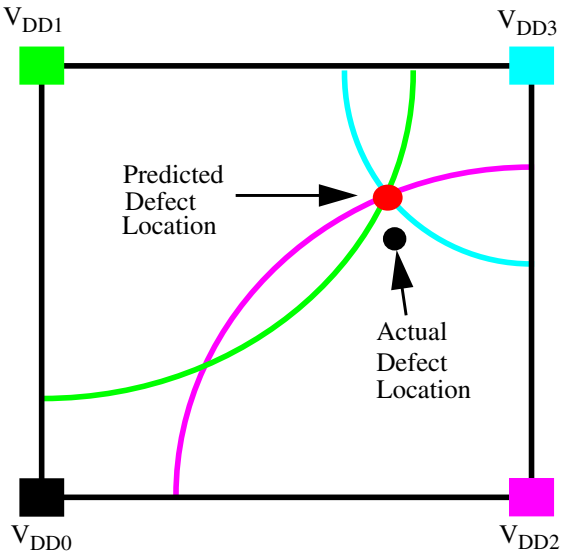

Figure 2. Application of resistance-based QSA model.

and k_i represent the x and y coordinates of the center of the *ith* circle. The centers of the circles The three circle equations are related to corresponding equations from the set described by Eq. 2 through the R_{eqi}. The choice of R_{eqi}, or equivalently, the choice of the supply pads to be used in the triangulation procedure is based on two criteria. First, the supply pads are sorted according to the magnitude of their corresponding I_{DDQ}. The supply pad, *j*, with the largest I_{DDQ} is selected followed by two orthogonally adjacent supply pads to pad *j* sourcing the next two largest values. Note that this model is based on two simplifying assumptions: a uniform resistance-to-distance mapping function and a R_{eqj} value of 1 (or a negligible value for R_p). A uniform resistance-to-distance mapping function is used to describe power grids in which the equivalent resistance and Euclidean distance between any two points on the grid are proportional.

An example application of this method is shown in Figure 2. Three circles are shown whose centers are given by supply pads V_{DD1}, V_{DD2} and V_{DD3}. Since supply pad V_{DD3} defines the center of the circle with smallest radius, it is the supply pad with the largest I_{DDQ}. The circles have been scaled by a common factor, *k*, to a common point of intersection labeled as "Predicted Defect Location".

3.2 Weaknesses of the Resistance-based Model

Unfortunately, the assumptions given under the resistance-based model are not valid in many situations. Let's first consider the assumption that R_p is small relative to the R_{eqi}. Under this assumption, the measured quantities, I_i, are related to the R_{eqi} through the simplifications of Eq. 2

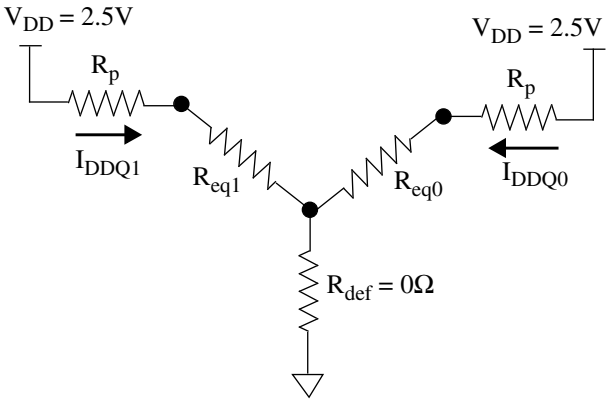

Figure 3. Simplified model of the defect and the equivalent resistances.

as given by Eq. 4. Therefore, the resistance-based QSA

$$R_{eqi} = \frac{I_j}{I_i} \times R_{eqj} + \underbrace{\left(\frac{I_j}{I_i} - 1\right) \times R_p}_{\text{If this term is negligible then}}$$

$$R_{eqi} \cong \frac{I_j}{I_i} \times R_{eqj} \quad \text{or} \quad R_{ratioi} = \frac{R_{eqi}}{R_{eqj}} \cong \frac{I_j}{I_i}$$

Eq. 4. Resistance Ratios

model assumes that the current ratios are inversely proportional to the resistance ratios. If the value of R_p is similar to or larger than the R_{eqi} values, the accuracy of the prediction is correspondingly reduced. In order to illustrate the impact of this term, the circuit shown in Figure 3 was simulated using SPICE over a range of R_p values from 0 to 10Ω. The values of R_{eq0} and R_{eq1} were set to 0.2Ω and 1.9Ω respectively (these values were chosen based on the analysis of the PPG described later). Figure 4 shows the behavior of the I_{DDQ}s from V_{DD0} and V_{DD1} shown in Figure 3. The currents from both supplies quickly deviate from their ideal values shown on the left to a constant related to the parallel resistance of the R_ps. In a similar fashion, the current ratio, I_0/I_1, quickly converges to 1 from its ideal value of 9.5, as shown in Figure 5.

The impact of R_p on the triangulation method is shown graphically in Figure 6. Here, three circles have been scaled by a factor *k* to a point of intersection. The initial radii derived from Eq. 2 are given as R_{req1} and R_{req2} with R_{eq3} = 1 used as the reference resistance. Under a zero R_p model, any point within the space confined by the four supply pads is a candidate. However, for non-zero values of R_p, candidate prediction points are confined to a smaller region, such as that defined by "Prediction Region" in the figure. In

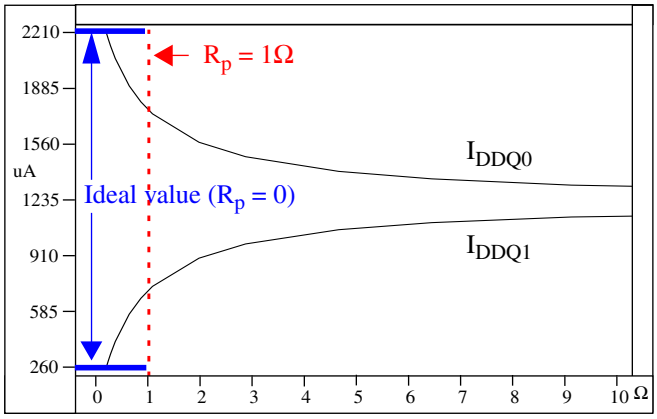

Figure 4. I_{DDQs} of the sources V_{DD0} and V_{DD1} vs. R_p.

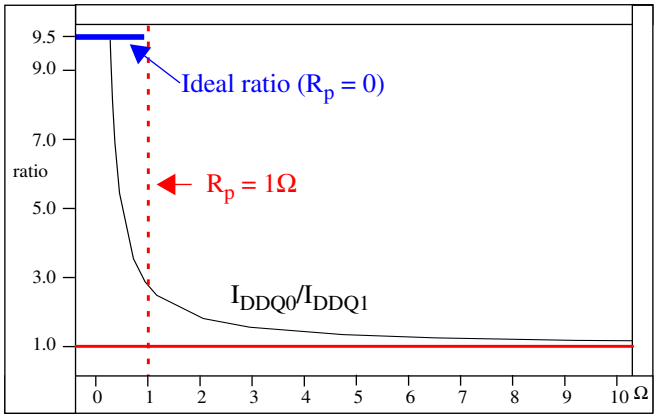

Figure 5. I_{dd0}/I_{dd1} ratio of I_{DDQs} in Figure 4 versus R_p.

other words, the current ratios become "diluted" by R_p, constraining the solution space of the circle equations (Eq. 3) to this region.

One solution to this problem is to remove one of the unknowns from Eq. 2. For example, if the actual value of R_{eqj} (the smallest resistance) is known, then the true values of R_{eqi} can be obtained using the current measurements independent of the value of R_p. One method of achieving this is to switch in a set of large resistors, e.g. 1KΩ, on the probe card, i.e. *increase* the value of the R_ps. Under the assumption that R_{def} (see Figure 1) is much larger than the R_{eqi} (a reasonable assumption for shorts not involving V_{DD} and GND metal rails directly), this configuration creates a voltage divider between the supply, the C4 contact point and GND. The value of the voltage at the C4 contact point for V_{DDj} allows R_{eqj} to be approximated. Unfortunately, modifying the probe card to allow this is difficult and expensive. A much simpler and more reliable technique that performs the equivalent function but is independent of R_{eqj} is defined for the new QSA model.

It should be noted that large values of R_p will still adversely affect the analysis even when R_{eqj} is known but only with respect to the precision of the measurements. As shown in Figure 5, the current ratios quickly approach 1 for reasonably small values of R_p, e.g. 10 Ωs. Therefore, larger R_p values require higher precision measurements under any proposed method.

The second weakness of the resistance-based QSA model is with regard to the uniform resistance-to-distance mapping function. Irregular supply topologies routed in multiple levels of metal are likely to be poorly modeled as uniform. In previous work, we proposed a mapping function based on resistance contours to deal with complex topologies. In this work, we propose a second strategy based on the use of a current-ratio lookup table. Both techniques require simulations and characterization of the grid beforehand, and should be avoided, if possible, in cases

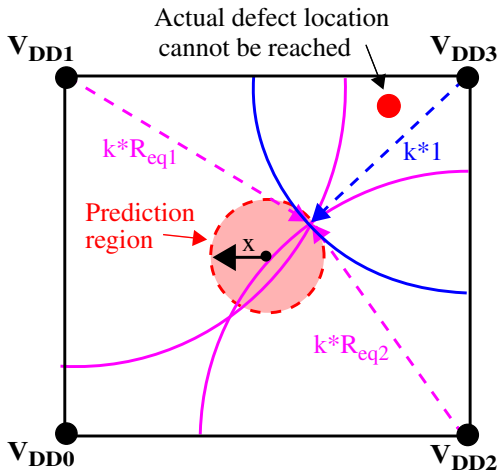

Figure 6. Impact of non-zero R_p on triangulation.

involving more regular topologies. This work is focused on deriving a simpler technique in these situations.

The topology of the PPG under investigation in this work fits between the totally regular and totally irregular extremes. The mapping function for it is not uniform but, because the physical structure of the grid is somewhat regular, it is possible to define two constants that characterize resistance per unit distance, one for points along the x axis and a second for points along the y axis.

3.3 PPG Physical and Electrical Characteristics

Figure 7(a) shows a portion of the PPG under analysis in this work, that is subsequently referred to as the Quad. The Quad occupies a 10,000 by 10,000 unit area and interfaces to a set of external power supplies through an area array of V_{DD} and GND C4 pads. A C4 pad is a solder bump for an area array I/O scheme. As indicated in the figure, there are four V_{DD} C4s and 6 GND C4s.

As shown in Figure 7(b), the grid itself is constructed over 4 layers of metal with metal 1 and 3 running vertically and metal 2 and 4 running horizontally. The C4s are connected to wide runners of vertical metal 5, indicated as m5

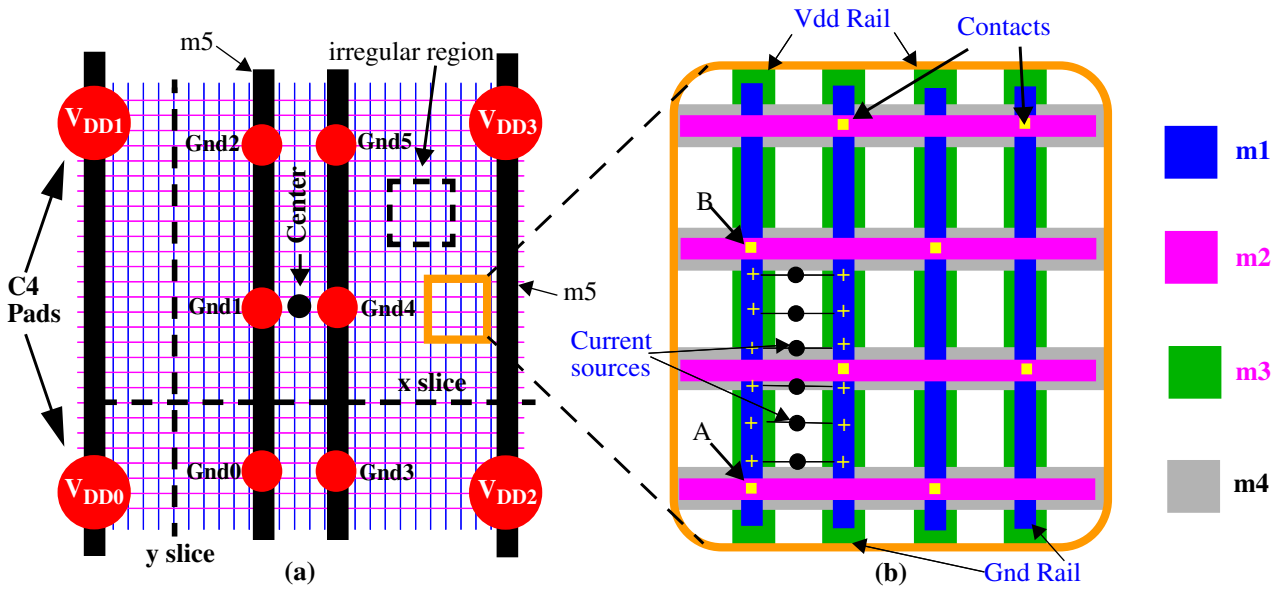

Figure 7. The "Quad": A portion of the PPG used in the simulation experiments.

in Figure 7(a), that are in turn connected to the m1-m4 grid. In each layer of metal, the V_{DD} and GND rails alternate. In the vertical direction, each metal 1 rail is separated by a distance of 432 units. The alternating vertical V_{DD} and GND rails are connected together using alternating horizontal metal runners. Stacked contacts are placed at the appropriate crossings of the horizontal and vertical rails. The grid is fairly regular except in the region labeled "irregular region" in the upper right corner of Figure 7(a). The metal 1 in this region of the layout varies from the regular pattern shown in Figure 7(b).

The R model of the Quad was obtained from an extraction script using parameters characterizing TSMC's 0.25µm process. 1Ω resistances were inserted between the power supplies and the R model of the grid to model the tester power supply(s) and probe card contact resistances to the chip. The combined resistance network contains approximately 27,000 resistors.

Figure 7(b) also shows a set of current sources that were inserted individually in a sequence of simulations as a means of evaluating the electrical behavior of the resistance model at the V_{DD} C4s. The current sources, which model the presence of a shorting defect, were placed at regular intervals between metal 1 V_{DD} and GND runners. An equivalent resistance model of the Quad is shown in Figure 8 with one of the current sources modeled. The four grid equivalent resistances, R_{geqi}, in the upper portion of the figure are the source of resistance variation as seen from the power supplies, as the current source is moved in the layout. The strength of the correspondence of these resistances to the position of the defect determines the accuracy of the triangulation procedure used in QSA. It is therefore prudent to evaluate this relationship for the Quad.

First it should be noted that the resistance model of the grid is actually three dimensional. This can be modeled as R_z and R_{xy} as shown on the right side of Figure 8. R_z adversely impacts the accuracy of the triangulation procedure for the same reasons given earlier for R_p. To make matters worse, the resistance variation over small vertical intervals of the Quad, e.g., along the interval between two contact points in metal 1, is on order with the variation across the entire Quad. For example, the segment length given between points A and B in Figure 7(b) is approximately 630 units. Using the metal 1 resistance parameter for TSMC's 0.25µm process yields a value of 5.6Ω. Therefore, in metal 1 alone, the resistance varies from 0Ω at the contact to 5.6 || 5.6 = 2.8Ω. On the other hand, the average resistance from the center of the grid (shown in Figure 7(a)) to any of the V_{DD}s (distance of ~7,000 units) is less than 6Ω. The increasing width of the metal runners from metal 1 to metal 5 is responsible for these resistance to distance anomalies. This discouraging result prompted us to explore the behavior of the other basic network variables, V_{def} (the voltage at the defect site) and the $I_{DDQ}s$ at the V_{DD} C4s.

A set of approximately 2,600 SPICE simulation experiments were run on the Quad. In each of these, a 20mA current source was placed between metal 1 V_{DD} and GND rails at different locations in the layout. Figure 9 shows the values obtained for R_{eq0} and I_0 at V_{DD0} and V_{def} (the current source's terminal voltage at the connection point on the metal 1 V_{DD} rail) for a set of simulations run along the lines identified as x-slice and y-slice in Figure 7(a). The R_{eq0} values were computed using Eq. 5. It is clear from

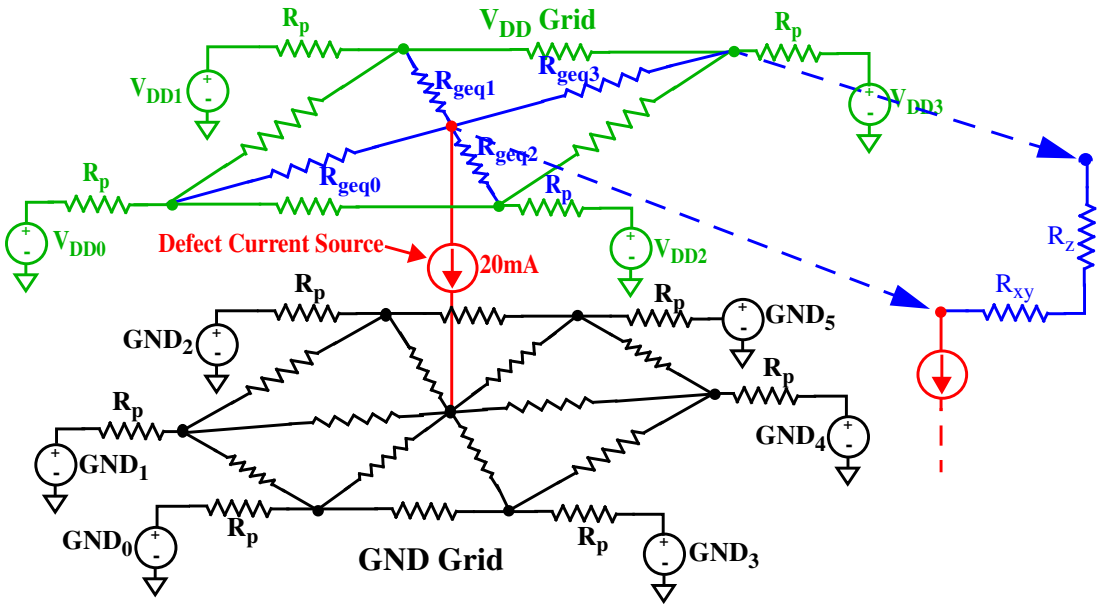

Figure 8. Model for the equivalent resistance network with the defect modeled as a current source.

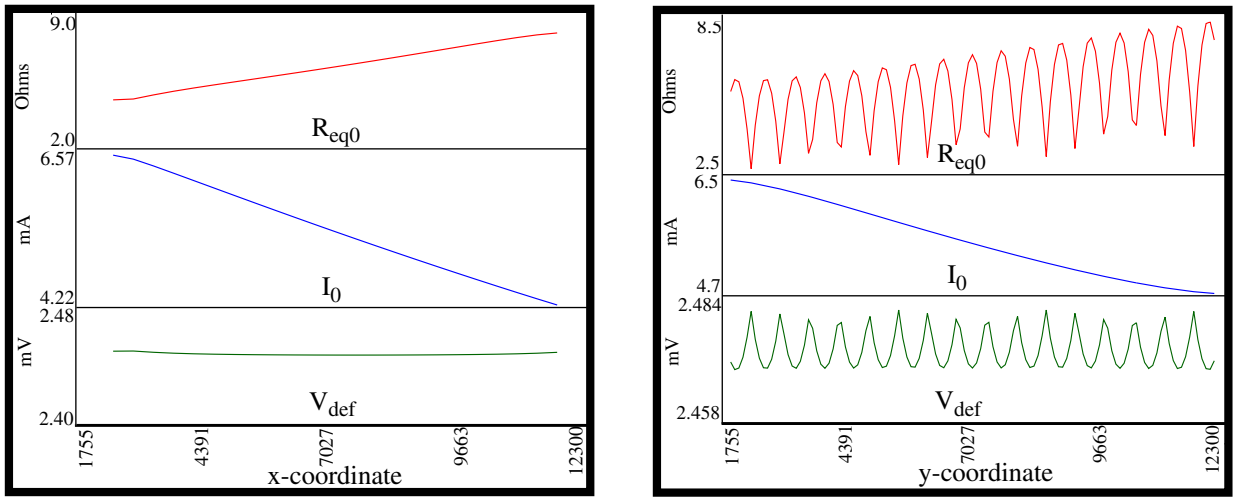

Figure 9. Variations in network variables along an x-slice (left) and a y-slice (right).

$$R_{eq0} = \frac{(V_{DD} - V_{defxy})}{I_0}$$

V_{DD} = 2.5V
V_{defxy} = voltage at the defect site (x,y)
I_0 = current through V_{DD0}

Eq. 5. Equivalent Resistance Definition.

these graphs that the variations in R_{eq0} and V_{def} along the *y* dimension are significantly larger than those along the *x* dimension. In contrast, the currents are well behaved along either dimension. The staggered arrangement of V_{DD} and GND grids, as shown in Figure 7(b), cause the *total* resistance between V_{DD} and GND (not shown) to change slowly across the grid, through the exchange of nearly equal resistance fragments between the V_{DD} and GND grids. This keeps the currents well behaved while the resistances to, and voltages at the defect site oscillate inversely with each other.

Another useful view of the behavior of these network variables is through contour plots. A line within a contour plot is defined as the parameter values over which the value of the function remains constant. Contours are particularly useful when data is to be fit to a function. Figures 10 and 11 show the equivalent resistance and current contours of the Quad for V_{DD0}. The parameters on the x and y axes corre-

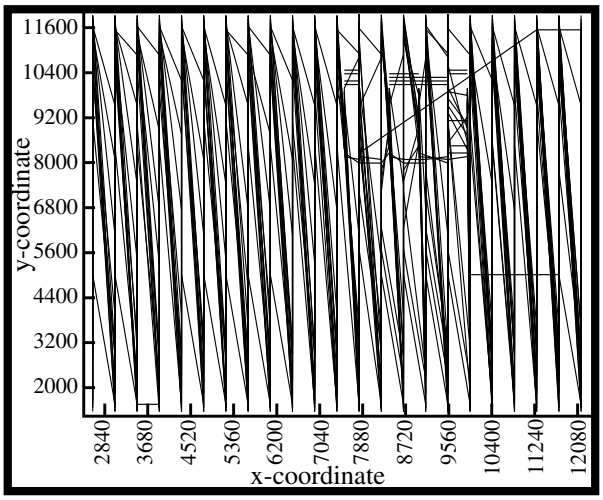

Figure 10. R_{eq0} contour plot of the Quad.

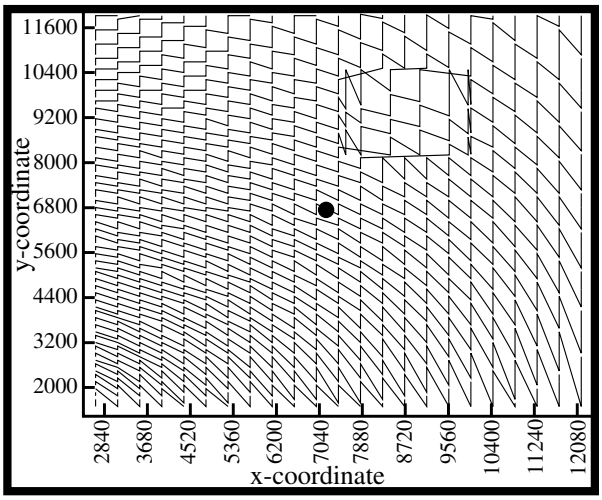

Figure 12. I_0/I_1 contour plot of the Quad.

spond to the (*x*,*y*) coordinates of the Quad as shown in Figure 7(a). It is clear that the equivalent resistance contour plot is difficult to make use of. The same is true of the V_{def} contour plot (not shown). In contrast, the current contours are well characterized as elliptical, (except for a region in the upper right hand corner, identified as "irregular region" given earlier in reference to Figure 7(a)). Similar patterns are present in the contour plots for the other V_{DD}s.

Therefore, a diagnostic method based on currents is likely to yield the best results. However, the disadvantage of using the currents directly is the dependency created between the value of defect's shorting current and the distance mapping procedure. This issue will be revisited in Section 4.0 when the details of the method are presented. Current ratios are an alternative that reduce this dependency since different values of defect current are reflected as the same ratio in the C4 I_{DDQ}s.

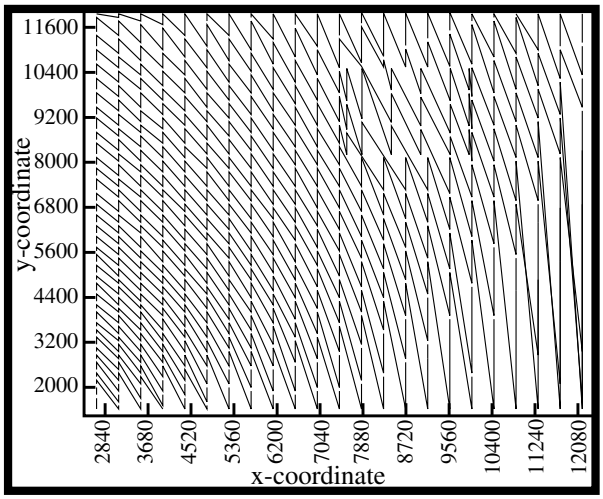

Figure 11. I_0 contour plot of the Quad.

The contour plot for I_0/I_1 is shown in Figure 12. Similar to the I_0 contour plot, the contour lines are well behaved. However, the elliptical curves characterizing the I_0 plot now appear as hyperbolic curves. The set or "family" of hyperbolic curves is centered at the midpoint between the position of V_{DD0} (lower left) and V_{DD1} (upper left). The contour curve that passes through this point on the y axis is nearly linear along this line to the center of the Quad (shown by the 'dot' in the center of the figure). This curve defines the points where the current ratios between V_{DD0} and V_{DD1} are 1. The I_0/I_1 extend downward to a maximum in the lower left corner. This maximum is not infinity since the R_z component of resistance between a point in metal 1 below V_{DD0} is non-zero. It is important to know this maximum value for the same reasons it is important to know R_{eqj} from the discussion in Section 3.2. We will soon describe an inexpensive DFT strategy that allows the maximum current ratio to be determined accurately. Let's first turn our attention to fitting the contours in Figure 12 to a family of hyperbolas.

4.0 The Current Ratio Model for QSA

Figures 13 and 14 show the I_0/I_1 and I_0/I_2 contour plots from the lower left quarter of the Quad. As noted above, the curve along the top of Figure 13 and the curve on the right in Figure 14 are the curves defined with a current ratio of unity. In order to fit these curves to a family of hyperbolas, it is necessary to first derive the parameters of the hyperbolas, *a* and *b*, as given by Eq. 6.

Figure 15 graphically defines the parameters, *a* and *b*, as well as an additional parameter, *c*, that plays an important role in our analysis by defining the relationship between the family of hyperbolas shown in Figures 13 and 14. Note that the hyperbolas given in Figure 13 are of the

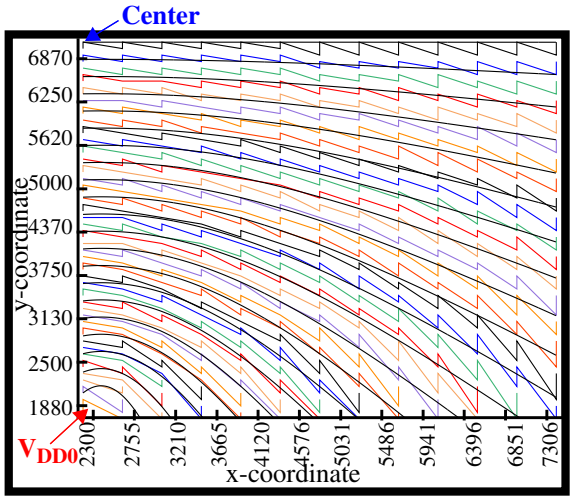

Figure 13. I_0/I_1 current ratio contours and hyperbolic curves for lower left quadrant of Quad.

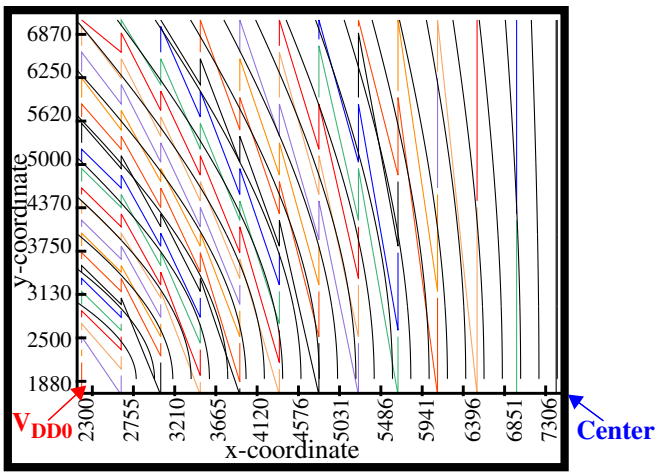

Figure 14. I_0/I_2 current ratio contours and hyperbolic curves for lower left quadrant of Quad.

$$\frac{(x-h)^2}{a^2} - \frac{(y-k)^2}{b^2} = 1$$

Eq. 6. Equation of a hyperbola.

vertical type, defined by inverting the signs of the two terms on the left hand side of Eq. 6. Other defining characteristics of the hyperbolas include F_1 and F_2, the foci of the hyperbolas. These points represent the (x,y) positions of the C4 V_{DDs} in our analysis. The last two parameters, h and k, allow the center of the hyperbola to be shifted away from the origin. In our analysis, the center of the hyperbolas is the midpoint between the C4 V_{DD}s (see Figures 13 and 14).

Under these definitions, both a and b need to be defined for each hyperbola in the family. However, Eq. 7 gives an alternative formulation of the hyperbola where b^2 has been replaced by $(c^2 - a^2)$. Since c is fixed for all curves (the

$$\frac{(x-h)^2}{a^2} - \frac{(y-k)^2}{c^2-a^2} = 1$$

Eq. 7. Alternative expression of a hyperbola.

(x,y) coordinate of the C4 supply pad), this makes b dependent on a. Therefore, only a needs to be defined. Note that a is the point at which the hyperbola defining the current ratio given by a intersects the x axis.

Without loss of generality, let's consider the horizontal I_0/I_2 hyperbolas. It is clear that a varies from 0, at the midpoint between V_{DD0} and V_{DD2}, to some maximum value, at a point directly underneath V_{DD0}. The current ratios at points along this line vary from 1 to some value less than

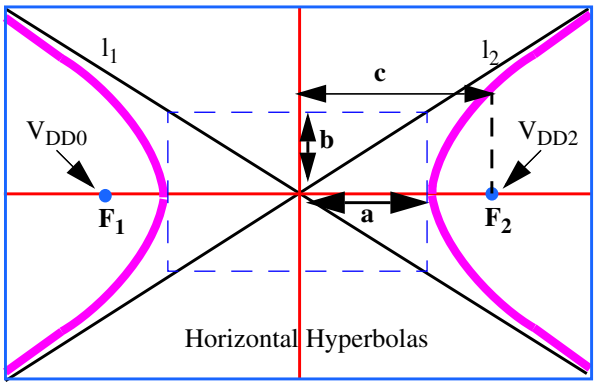

Figure 15. Definitions of the hyperbola parameters

infinity (the maximum current ratio), as discussed in the previous section. If this maximum current ratio is known, then the function that defines a can be written as given by Eq. 8, whose parameters are defined in Figure 16. Here,

$$\frac{I_0}{I_2} = \frac{R_{eqT} \times (L-m) + L \times R_P}{m \times R_T + L \times R_P}$$

and

$$a = \frac{L}{2} - m$$

Substituting and solving for a yields

$$a = \frac{L}{2} - \frac{L}{R_{eqT}} \left(\frac{R_P \left(1 - \frac{I_0}{I_2}\right) + R_{eqT}}{\left(1 + \frac{I_0}{I_2}\right)} \right)$$

Eq. 8. Expression for a

V_{def} represents the voltage at the defect site. R_{eqT} (total

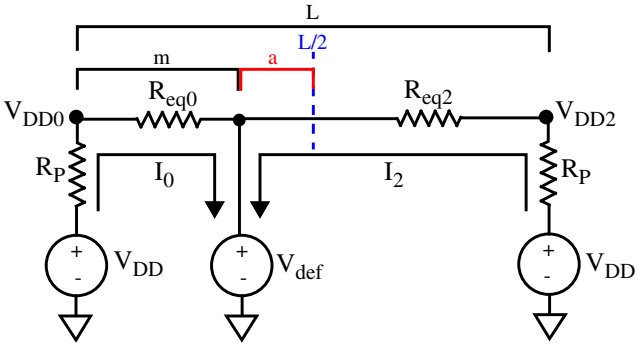

Figure 16. Model for parameter *a* for hyperbolas.

resistance) is equal to the sum of the equivalent resistances between the defect site and each of the two V_{DD} pads. R_P is the probe card's resistance. As pointed out earlier, R_{eq0} and R_{eq2}, and therefore R_{eqT}, can not be obtained in the defective chip.

However, under the special case where the defect shown in Figure 16 is along a line between V_{DD0} and V_{DD2}, we can obtain a close approximation of R_{eqT} through the use of Calibration transistors at known points in the design, as shown in Figure 17. The source and drain of the Calibration transistors connect to V_{DD} and GND in metal 1 and provide a way to conditionally short these nodes together. Since the maximum current ratio is sought, the best position for the Calibration transistors are directly underneath the C4 supply pads, e.g., V_{DD0}, at the lowest resistance position. Scan chain flip-flops are used to control the state of the transistors. The chip is first placed into a state that does not provoke the defect and the appropriate Calibration transistor is turned on. (The relevant Calibration transistor is determined by the C4 pad that draws the maximum current under a circuit state that provokes the short.) The measured values of I_0 and I_2 along with the known values of L, R_P and a are used to derive R_{eqT} as given by Eq. 9 (which is Eq. 8 solved for R_{eqT}). The R_{eqT}

$$R_{eqT} = \frac{LR_P\left(1 - \frac{I_0}{I_2}\right)}{a\left(\frac{I_0}{I_2} + 1\right) - L}$$

Eq. 9. Expression for R_{eqT}

obtained this way can then be substituted into Eq. 8 (since the sum of R_{eq0} and R_{eq2} remains constant for both cases) and the value of a obtained, this time, using the values of I_0

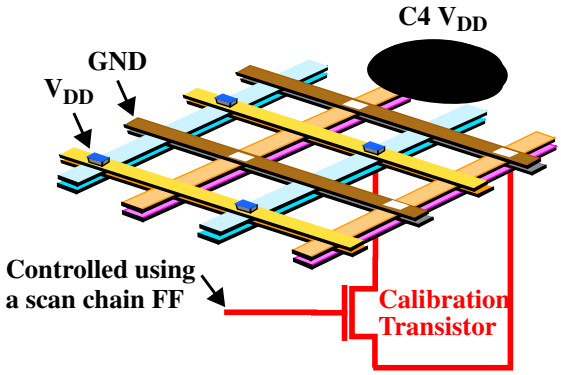

Figure 17. Calibration Transistor.

and I_2 measured under the shorting state of the circuit. The value of b is then obtained from Eq. 10.

$$b^2 = c^2 - a^2 = \left(\frac{L}{2}\right)^2 - a^2$$

Eq. 10. Expression for *b*

Although it is not immediately obvious, the values of R_{eqT} and, more importantly, R_P, are not actually needed. After the substitutions are made, these terms cancel out since they are present and identical in both forms of the expression. (The final form of the expression is given in Section 5.0). Thus, a nice feature of this calibration technique is that it is independent of R_P, which is likely to vary from touch-down to touch-down of the probe card. The alternative strategy, of computing the maximum current ratio from simulation experiments, is less attractive because of this.

Two elements have not yet been addressed. We have not yet factored in the differences in the resistance-to-distance factors for the x and y dimensions nor have we addressed leakage current effects. The latter issue was dealt with in previous work using a scheme based on regression analysis [7]. Although calibrating for leakage is clearly an important issue, we do not focus on it in this work because of space limitations. The limited number of experiments conducted thus far involving leakage indicate that it does not affect the accuracy of the predictions. The same is true for experiments conducted using different values of defect current. Current ratios are naturally robust to these variables but a quantitative analysis of their impact remains to be determined and will be addressed in a future work.

The second issue was identified as a weakness of the original resistance-based QSA model in Section 3.2. A clue to determining how to calibrate for this effect is given in Figure 11. The elliptical shape of the contours shown in the figure is due to the different resistance-to-distance factors which characterize the x and y dimensions of this PPG (otherwise they would be circles). The difference in the values

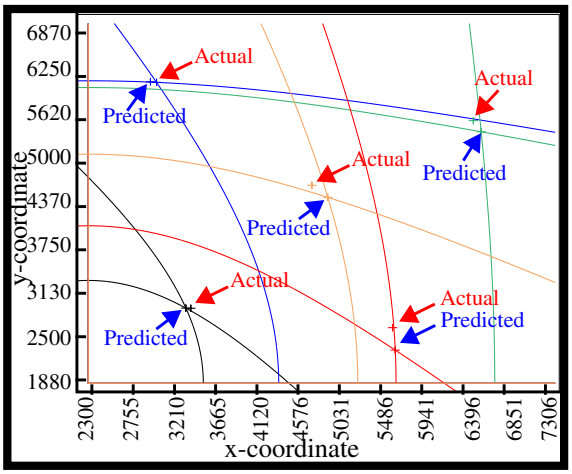

Figure 18. Application of the new QSA model to the lower left quarter of the Quad

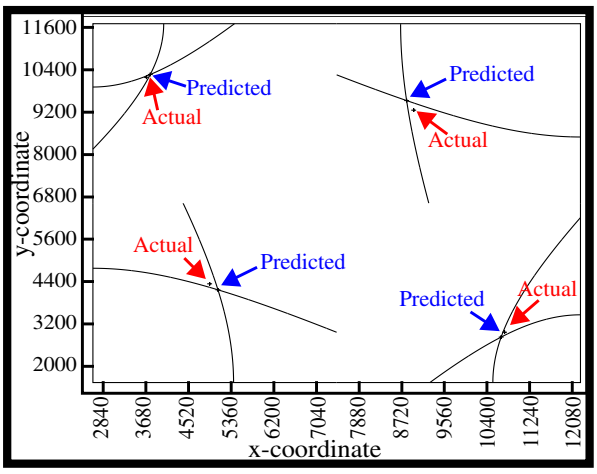

Figure 19. Application of the new QSA model to all quarters of the Quad.

of the resistance-to-distance factors appears to change only the curvature of the hyperbolas and has little impact on parameter a as described above. It is straightforward to derive a factor that expresses the difference in resistance-to-distance along the x and y dimensions using the Calibration transistor results. The factor derived as the ratio of the two current ratios expresses the difference. In our experiments, we determined that multiplying one of the b parameters by this factor yields excellent results. For example, if the resistance-to-distance factor along the y axis is 0.65 times the resistance-to-distance factor along the x axis, multiplying the b parameter for the vertically oriented hyperbolas (e.g., the V_{DD0}-V_{DD1} curves) by 0.65 reduces the error in the predictions significantly. We are currently working on deriving the analytical expressions that relate this factor to the parameters of the hyperbolas.

4.1 The QSA Procedure

The procedure to localize a defect follows from the discussion given in the previous section. Once a chip is identified as defective, e.g. from a Stuck-At or I_{DDQ} go-nogo test, the following tests are performed during the diagnostic procedure. First, the chip is set to a state that provokes the defect and the individual I_{DDQ} values are measured. The C4 pad, j, sourcing the largest I_{DDQ} and two orthogonally adjacent C4 pads, x and y, are identified (as described in Section 3.0). The chip is then put into a state that doesn't provoke the defect. The Calibration transistor for the *jth* C4 pad is turned on and the current ratios I_j/I_x and I_j/I_y computed. The values of R_{eqTx} and R_{eqTy} are computed using Eq. 9. Using these values and the current ratios obtained under the shorted state, the values of the parameters, a_x and a_y are computed using Eq. 8 and then the values of parameters b_x and b_y using Eq. 10. (The b_x or b_y parameter is also scaled by the distance-to-resistance factor as described in the previous section). These parameters define both the position and shape of one hyperbola from each family. The intersection of these two hyperbolae gives the predicted location of the defect.

Figures 18 and 19 show examples of this procedure applied using defects inserted in the lower left hand quarter of the Quad (left) and each of the four quarters of the Quad (right). The error metric we adopt is to compute the shortest distance between the predicted and actual location (prediction error). This distance can be fairly compared with the length along the diagonal of the "predicted into" region (normalization factor). Since the width and length of the "predicted into" region is always a 5,000 by 5,000 unit area, the diagonal distance is 7,071. This permits the error to be expressed as a percentage given by the ratio of the prediction error and the normalization factor (times 100). For the cases shown in the figure, the error is less than 350 units or 5%.

5.0 Experimental Results

As indicated above, the calculation of the a parameters to the two hyperbolas can be done independent of R_{eqT} and R_P. The simplified expression for a is given by Eq. 11. Note that this expression also allows for the Calibration transistor to be offset from the exact position of the C4 V_{DD} under which it is placed.

This algorithm was applied to the data obtained from 2,600 simulation experiments used to generate the contours shown in Section 3.3. A three dimensional error map plotting the prediction error against the (x,y) coordinate is shown in Figures 20 and 21. Figure 20 shows the prediction error for the lower left quarter of the Quad while Figure 21 gives it for the entire Quad. The worst case and average case prediction error is 574 and 207 units respectively.

The smallest prediction error occurs at points in the Quad where the current ratios are close to unity. The pre-

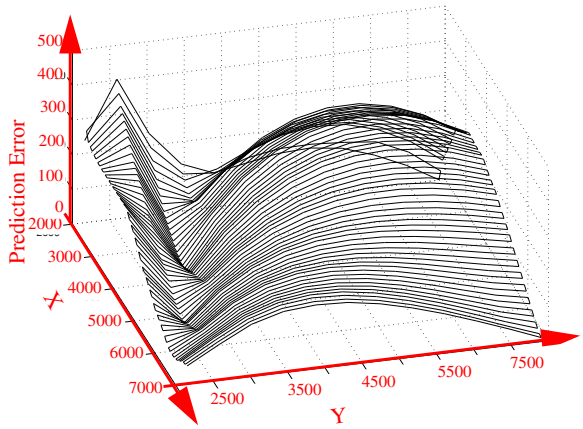

Figure 20. 3-D plot showing the prediction error for the lower left quarter of the Quad.

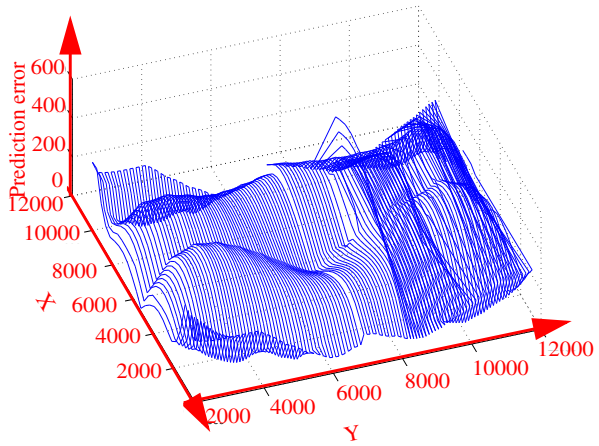

Figure 21. 3-D plot showing the prediction error for the whole Quad.

$$a' = -\{(CR_{ct} \times x_t) + x_t - (CR_d \times CR_{ct} \times x_t) + (CR_d \times L) - (CR_d \times x_t) - (CR_{ct} \times L)\} / \{(1 + CR_d) \times (CR_{ct} - 1)\}$$

where,

CR_{ct} = current ratio from the calibration transistor

CR_d = current ratio under defect provoking state

x_t = Calibration transistor offset from C4 V_{DD}

L= distance between two adjacent C4 V_{DD}s

and a is given by: $a = \frac{L}{2} - a'$

Eq. 11. Reformulation of a without R_{eqT} and R_p.

diction error tends to increase near the pads where the current ratio contours are very sharp and not approximated well by the hyperbolas. The smooth contour in the prediction error surface suggests that our model is not complete. We suspect it is related to our treatment of the resistance-to-distance factors described earlier.

The highest prediction errors occur in the irregular region of the Quad identified in Figure 7. This is expected since the extra and displaced metal 1 runners cause a local change in the resistance contour that cannot be tracked by the hyperbolas. The average prediction error in this region increases by approximately 50 units.

6.0 Conclusions

Simulations on a production power grid were used to demonstrate weaknesses in our previously derived resistance-based Quiescent Signal Analysis model. A new current-ratio-based QSA model was derived to address the shortcoming of the original model. A DFT structure that consists of a Calibration transistor and a scan chain flip-flop is proposed as a calibration technique to circumvent inaccuracies introduced by the probe card resistance and non-uniform resistance-to-distance mapping functions. Hyperbolas are shown to be a good fit of the current ratio contours and expressions are derived that yield good approximations of their parameters. The worst case and average case prediction error occurring in a set of 2,600 experiments was 8.1% and 3%, respectively. Simulations of a larger portion of the PPG are underway, as well as work on unresolved issues related to modeling, leakage currents and non-uniform resistance-to-distance mapping functions.

Acknowledgments

We would like to thank Dr. Anne Gattiker and Dr. Sani Nassif at IBM Austin Research Lab for their support of this research.

References

[1] T.W.Williams, R.H.Dennard, R.Kapur, M.R.Mercer & W.Maly, "I_{DDQ} test: Sensitivity Analysis of Scaling", In proceedings *International Test Conference* 1996, pp.786-792.

[2] A.E.Gattiker and W.Maly, "Current Signatures", In proceeding VLSI Test Symposium, 1996, pp.112-117.

[3] C. Thibeault, "On the Comparison of Delta IDDQ and IDDQ test", In proceedings 17th IEEE VLSI Test Symposium, 1999, pp. 143-150.

[4] Peter Maxwell, Pete O'Neill, Rob Aitken, Roland Dudley, Neal Jaarsma, Minh Quach, Don Wiseman, "Current Ratios: A self-Scaling Technique for Production IDDQ Testing", In proceedings International Test Conference, 1999, pp.738-746.

[5] Jim Plusquellic, "IC Diagnosis Using Multiple Supply Pad IDDQs" IEEE Design and Test, Special Issue on Diagnosis, Oct 2000.

[6] Chintan Patel and Jim Plusquellic, "A Process and Technology-Tolerant IDDQ Method for IC Diagnosis" in proceedings VLSI Test Symposium, 2001, pp. 145-150.

[7] Christopher L.Henderson and Jerry M.Soden, "Signature Analysis for IC Diagnosis and Failure Analysis", In proceedings International Test Conference, 1997, pp.310-318.

[8] C. Thibeault, L. Boisvert, "Diagnosis method based on delta IDDQ probabilistic signatures: Experimental results", In proceedings International Test Conference, 1998, pp.1019-1026.